

PCCP

Accepted Manuscript



This is an *Accepted Manuscript*, which has been through the Royal Society of Chemistry peer review process and has been accepted for publication.

Accepted Manuscripts are published online shortly after acceptance, before technical editing, formatting and proof reading. Using this free service, authors can make their results available to the community, in citable form, before we publish the edited article. We will replace this *Accepted Manuscript* with the edited and formatted *Advance Article* as soon as it is available.

You can find more information about *Accepted Manuscripts* in the [Information for Authors](#).

Please note that technical editing may introduce minor changes to the text and/or graphics, which may alter content. The journal's standard [Terms & Conditions](#) and the [Ethical guidelines](#) still apply. In no event shall the Royal Society of Chemistry be held responsible for any errors or omissions in this *Accepted Manuscript* or any consequences arising from the use of any information it contains.



Physical Chemistry Chemical Physics

ARTICLE

Influence of halide precursor type and its composition on the electronic properties of vacuum deposited perovskite films†

Tae Gun Kim,^{ab} Sung Won Seo,^{ab} Hyuksang Kwon,^a Junhee Hahn,^a and Jeong Won Kim^{*ab}

Received 00th January 20xx,
Accepted 00th January 20xx

DOI: 10.1039/x0xx00000x

www.rsc.org/

We fabricate mixed halide perovskite films by dual-source vacuum deposition of PbX_2 ($X = \text{Cl}, \text{Br}, \text{and I}$) and methyl ammonium iodide (MAI) precursors with various deposition ratios. The vacuum deposition is an optimal way of film fabrication because it gives a uniform perovskite film free from contamination such as lead metallic phase, residual solvent, and moisture. The ionization potential and bandgap of $\text{MAPb}(\text{I}_{1-y}\text{Br}_y)_3$ film are controlled by halide composition and lattice constant change. In contrast, $\text{MAPb}(\text{I}_{1-y}\text{Cl}_y)_3$ film shows negligible difference from MAPbI_3 in structural and electronic properties, which is due to poor Cl incorporation in the film by the MAI removal during crystal formation. Excess supply of MAI is necessary to form a perovskite crystal structure. Based on the elemental stoichiometry analysis, the additional methyl ammonium cation with respect to Pb in the film plays a critical role in changing electron affinity and energy level alignment.

1. Introduction

Organic-inorganic halide perovskite has gained intensive attraction as highly efficient photovoltaic materials due to their strong optical absorption, long exciton lifetime, high electrical conductivity, and easy fabrication process.¹⁻⁵ Inorganic divalent metal (e.g. Pb^{2+} , Sn^{2+} , and Ge^{2+}) and halide anion (e.g. Cl^- , Br^- , and I^-) form octahedral shape of perovskite lattice frame while organic amines such as CH_3NH_3^+ (Methyl ammonium cation, MA^+) and $\text{HC}(\text{NH}_2)_2^+$ (Formamidinium cation, FA^+) play an electrostatical neutralization.⁶ Thus one of fundamental advantages in the perovskite materials is bandgap (E_g) tunability from red to blue depending on their composition and stoichiometry of cations and anions.⁷⁻⁹ This enables us to design an efficient photovoltaic cell with high open circuit voltage (V_{oc}) or tandem structure.

Most perovskite solar cells have so far been fabricated by solution based spin-coating^{10,11} and dipping¹² methods. These methods realize device fabrication on large scale at low price.¹³ However, they are accompanied by various concerns of process condition such as precursor concentration, suitable solvent, spin-coating condition, conversion time, and annealing temperature.^{4, 14} Furthermore, the surface of solution-processed perovskite films usually shows non-uniform and rough morphology. As a result, the deterioration in V_{oc} and

short circuit current (J_{sc}), and the direct shunting path are generated.^{15, 16} To tackle those weak points, Snaith's group proposed a dual-source vacuum deposition method for mixed halide perovskite ($\text{MAPbI}_{3-y}\text{Cl}_y$) solar cells. They have reached the solar cell efficiency of 12.3 % (maximum 15.4 %).¹⁶ The Cl mixed halide perovskite has been reported that it has longer carrier diffusion length and PL lifetime than a tri-iodide perovskite (MAPbI_3) by the passivation of trap states or extra doping.¹⁷⁻¹⁹ However, many people reported that the amount of Cl^- in the film might be negligible within the detection limit of energy-dispersive X-ray spectroscopy (EDX) and X-ray photoelectron spectroscopy (XPS).²⁰⁻²⁵ Thus the halide precursor type and its deposition ratio under vacuum would strongly influence film structure, stoichiometry, and electronic property of halide perovskite materials. Such information is a prerequisite for solar device optimization made of mixed halide perovskite, in particular of $\text{MAPb}(\text{I}_{1-y}\text{Br}_y)_3$ and $\text{MAPb}(\text{I}_{1-y}\text{Cl}_y)_3$.

Here, we have fabricated the mixed halide perovskite by co-evaporation of methyl ammonium iodide (MAI) and a lead halide (PbX_2 ; $X = \text{Cl}, \text{I}, \text{and Br}$) precursors under high vacuum. Right after the film preparation, the ionization potential (IP) and chemical composition of perovskite film surfaces are analysed by photoelectron spectroscopy without air exposure. Depending on the relative deposition ratio of the precursors, their bandgap, crystallinity, and surface morphology are also compared by UV-Vis absorption, XRD, and AFM. Vacuum processed films provide almost impurity-free information of stoichiometry and a smooth surface. While $\text{MAPb}(\text{I}_{1-y}\text{Cl}_y)_3$ shows very similar crystal structure and bandgap to MAPbI_3 irrespective of PbCl_2 deposition ratio, $\text{MAPb}(\text{I}_{1-y}\text{Br}_y)_3$ exhibits scalable properties with relative PbBr_2 precursor composition. Among the various deposition ratios of PbX_2 and MAI, excess

^a Korea Research Institute of Standards and Science (KRISS), 267 Gajeong-ro, Daejeon 305-340, Korea

^b Korea University of Science and Technology (UST), 206 Gajeong-ro, Daejeon 305-350, Korea

* E-mail: jeongwonk@kriss.re.kr

† Electronic Supplementary Information (ESI) available: [Additional UPS, XPS, XRD and AFM data of pristine MAI, PbI_2 , PbBr_2 , and PbCl_2]. See DOI: 10.1039/x0xx00000x

ARTICLE

amount of MAI is necessary to form a perovskite crystal structure. As a result, the excess amount of MA⁺ in the perovskite film strongly influences the IP and electron affinity (EA) of the film.

2. Experimental

Sample Preparation. PbI₂ (99%, Sigma-Aldrich), PbCl₂ (98%, Sigma-Aldrich), PbBr₂ (99.999%, Alfa-Aesar), and CH₃NH₃I (98%, TCI) were used without further purification as they were purchased. The PbX₂ (X= I, Cl, Br) and CH₃NH₃I were deposited by thermal co-evaporation on UV-ozone treated indium tin oxide (ITO). The total film thickness was kept constant at 30±2 nm and the deposition rate on the order of 0.1 Å/sec. The film thickness and deposition rate were monitored by a quartz crystal microbalance, and they were verified by AFM afterward. During the deposition, the chamber pressure was maintained in the range of 10⁻⁵ mbar. After the deposition, the samples were transferred to an analysis chamber to measure photoelectron spectroscopy without exposing in air.

Photoelectron Spectroscopy Measurement. The base pressure of the analysis chamber was maintained under low 10⁻⁹ mbar. The ultraviolet and x-ray photoelectron spectroscopy (UPS and XPS) measurement were performed using a hemispherical electron energy analyser (RESOLVE 120, PSP). The UPS measurement used a He I (hν = 21.22 eV) discharge lamp as an excitation source with sample bias of -15 and -10 V for secondary electron cut-off and valence band region, respectively. The XPS measurement used a Mg Kα (hν = 1248.5 eV) without a monochromator. Energy resolutions were approximately 0.1 and 1.0 eV for UPS and XPS, respectively. The EF level was calibrated through Ar⁺ sputtered clean Au.

UV-Vis Absorption and XRD Measurement. UV-Vis absorption spectra were measured by a UV-Vis spectrometer (S-4100, Sinco) right after the photoelectron spectroscopy analysis. An ITO substrate spectrum was removed as a blank sample. XRD measurement was performed with a Cu Kα (λ = 0.154 nm) source (Rotaflex RU-200B, Rigaku). The XRD sample stage was rotated automatically during measurement and its scanning range was between 5 and 60 degrees with a step interval of 0.02 degree.

AFM Measurement. The perovskite film morphology and roughness were measured by AFM (XE-70, Park Systems) in non-contact mode with a tip of PPP-NCHR type. The images were collected at several different places over each sample.

3. Results and discussion

3.1 Film structure with precursor deposition ratio

XRD pattern refers to whether the halide-mixed perovskite film fabrication by vacuum deposition is successful as the MAPbI₃ perovskite structure has main diffraction peaks at 14.1°(110), 28.4°(220), and 43.2°(330).¹⁶ The XRD patterns for the manufactured films in the 2 theta/(deg.) range of 8-20° are

displayed in Fig. 1a-c. Surprisingly, a well-resolved perovskite peak at 14.1° is resolved even without post-heat treatment as long as the deposition ratio is appropriate. In Fig. 1a, the 12.6° peak is related to PbI₂ (001) formation, which is confirmed by the symbol, # in Fig. S1.^{26, 27} The PbI₂ peak decreases with increasing the MAI ratio, while MAPbI₃ peak (*) becomes dominant in Fig. 1a.

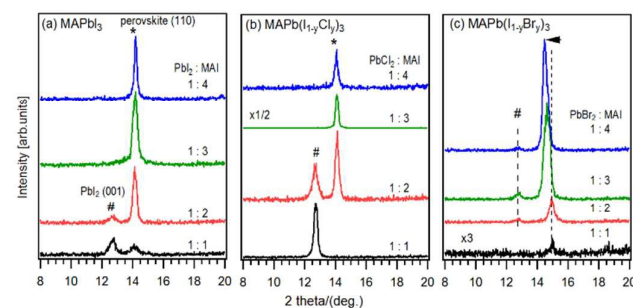


Fig. 1 XRD scans for the thin films of (a) MAPbI₃, (b) MAPb(I_{1-y}Cl)_y, (c) MAPb(I_{1-y}Br)_y. #: PbI₂ (001), *: MAPbI₃ perovskite (110).

When the PbCl₂ and MAI deposition ratio is 1:1, no diffraction peak evolves but for PbI₂ in Fig. 1b. The reaction of PbCl₂ and MAI triggers preferentially the exchange between Cl⁻ and I⁻ anions. Consequently, the PbI₂ and MAI rather than MAPb(I_{1-y}Cl)_y are produced,^{28, 29} and the MAI is not detected as it is removed into gas phase.³⁰ As the MAI deposition ratio increases, the MAPb(I_{1-y}Cl)_y peak becomes dominant. To avoid the formation of PbI₂ phase, one needs excess amount of MAI more than three times of PbX₂. This result clearly indicates that the relative deposition ratio between PbX₂ and MAI determines the purity of fabricated perovskite film. The production of high-purity perovskite film is of importance because the by-product such as PbI₂ can deteriorate the device performance.^{27, 31} One more interesting observation is that the same perovskite peak at 14.1° is observed in either MAPb(I_{1-y}Cl)_y or MAPbI₃.³² But, it is absolutely different from the trichloride perovskite (MAPbCl₃) that represents the (110) diffraction peak at 15.6°.³³ This phenomenon indicates that the small amount of mixed Cl is not represented by (110) d-spacing shift in MAPb(I_{1-y}Cl)_y.

In the film of MAPb(I_{1-y}Br)_y in the Fig. 1c, the formation of PbI₂ is negligible throughout the relative deposition ratio. However, the perovskite peak becomes dominant under the excess ratio of MAI as in the previous films. The main peak for MAPb(I_{1-y}Br)_y films is shifted from 14.9° to 14.5° with the relative MAI ratio. The XRD peak shift in the low deg. direction is a consequence of the (110) d-spacing increment by 0.16 Å (Bragg's law). It can be simply explained that the I⁻ ion (0.206 nm) replaces the Br⁻ ion (0.182 nm) in the perovskite lattice site as the MAI ratio increases, whereas such lattice change is not present in the case of PbCl₂ in Fig. 1b. Furthermore, under PbCl₂ rich deposition, even the diffraction pattern for PbI₂ or MAPbI₃ does not appear (Fig. S1). Only excess amount of MAI triggers the perovskite production reaction.

3.2 Optical bandgap with precursor deposition ratio

The optical bandgap of the perovskite films with the ratio of PbX_2 and MAI precursors is measured by UV-Vis absorption spectrometer in Fig. S2, and its values are exhibited in Fig. 2. The E_g of MAPbI_3 film is in the range 1.57-1.59 eV, which is similar to previous reported ones for solution based MAPbI_3 films (1.55-1.6 eV).^{8, 9, 34-37} Interestingly, the $\text{MAPb}(\text{I}_{1-y}\text{Cl}_y)_3$ films also show a similar range of E_g values, which is reasonably assumed from the similar crystallographic characteristics observed by XRD in Fig. 1. But the subtle increase in E_g for $\text{MAPb}(\text{I}_{1-y}\text{Cl}_y)_3$ is possibly due to partial substitution of I⁻. On the other hand, the Br mixed perovskite films have larger E_g 's than MAPbI_3 . This is because the mixed (hetero) halide causes a slight lattice distortion and structural change of the perovskite as shown in Fig. 1c. This observation is consistent with previous report.³⁸ But the E_g change with the relative deposition ratio is marginal. According to the recent report, the E_g variation can be explained by the grain size change of perovskite material according to different MAI concentration as a consequent of quantum confinement effect.³⁹ But, in the present study, this effect is ruled out because the FWHM of the XRD peaks for perovskite (110) is not changed with the MAI concentration.

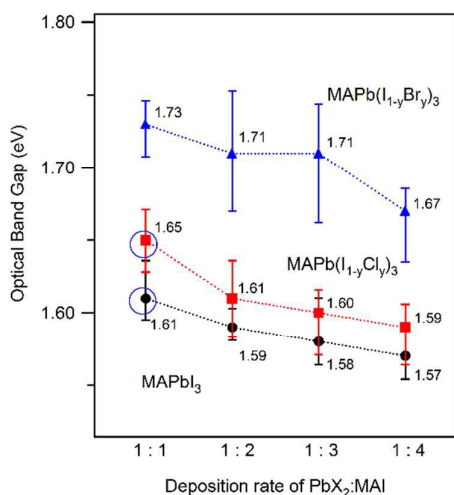


Fig. 2 Optical bandgaps of mixed halide perovskite films made by various deposition ratios. Blue circles indicate the points where a mixture of perovskite film and by-product is observed by XRD. The error bars correspond to the uncertainties in the determination of absorption offset values.

3.3 Ionization potential with halide composition

Fig. 3a-c shows UPS spectra as a function of deposition ratio between PbX_2 and MAI precursors from 1:1 to 1:4. The valence band maxima with respect to the vacuum level are determined by linear fitting of the last peak slope and the background. The corresponding IP values are marked by the vertical bars on the binding energy (BE) scale and summarized in Fig. 3d. The IP, one of the intrinsic properties of materials, directly affects the energy level alignment at interface, the associated photo-

induced carrier (exciton) transfer or separation, and charge collection at each electrode.^{40, 41} Fig. 3d shows that the IP values decrease with the relative MAI deposition ratio regardless of the type of PbX_2 . On the bottom of the Fig. 3d, when the deposition ratios of PbI_2 and MAI are 1:3 and 1:4, the IP of MAPbI_3 is in the range of reported IP values, 5.40-5.70 eV for solution processed tri-iodide perovskite.³⁴ As noticed by crystallization condition in Fig. 1, a certain ratio between MAI and PbI_2 precursor is needed to fabricate a MAPbI_3 film of desirable electronic property by dual-source vacuum deposition. Otherwise, unwanted by-product of PbI_2 phase remains. Indeed, when the deposition ratio is 1:1 in Fig. 3a and b, its electronic band structure observed by UPS shows the very similar feature of PbI_2 precursor in Fig. S3. On the other hand, when the deposition ratio is 1:4, the UPS spectral shapes of both Fig. 3a and b look similar. Thus, the same (110) d-spacing, similar bandgap and electronic structure strongly indicate that MAPbI_3 and $\text{MAPb}(\text{I}_{1-y}\text{Cl}_y)_3$ have the same crystal structure even though they are manufactured of different precursors.

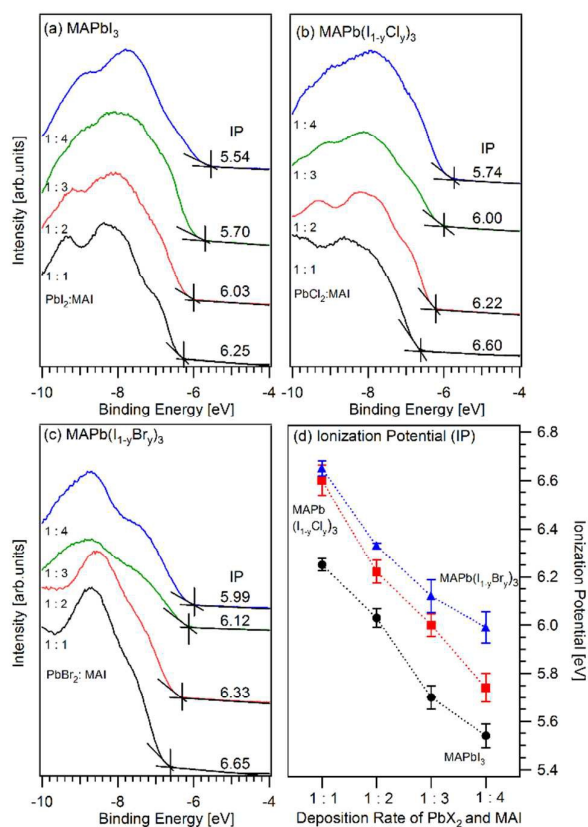


Fig. 3 UPS valence band spectra as a function of deposition ratio between PbX_2 and MAI precursors for (a) MAPbI_3 , (b) $\text{MAPb}(\text{I}_{1-y}\text{Cl}_y)_3$, (c) $\text{MAPb}(\text{I}_{1-y}\text{Br}_y)_3$. Binding energy scale is referenced to vacuum level ($E_{\text{vac}} = 0$ eV). Each ionization potential (IP) value is summarized in (d).

On the other hand, the IPs for mixed halide perovskite films are clearly higher than that of pure MAPbI_3 . It is known that the frontier valence band position is sensitive to each halide p-

orbital in organic halide perovskite.^{42,43} The low IP of MAPbI₃ can be understood by the highest polarizability of p orbital of I⁻ ion and the smallest electronegativity difference from Pb atom among the three types of halide anions.⁷ This makes a series of different ionic bond strength, Pb-I < Pb-Br < Pb-Cl in perovskite structure. From this point of view, the MAPb(I_{1-y}Cl_y)₃ should show higher IP than MAPb(I_{1-y}Br_y)₃ because the PbCl₂ has the highest ionic bond strength and IP among the lead halides (7.80 eV; Fig. S3). However, the IP values in the Fig. 3d are inconsistent with our expectation. We suspect that the actual stoichiometry is not conserved as it is deposited. In addition, the PbCl₂ deposition ratio does not affect the IP as much as the PbBr₂ precursors, which is consistent with previous report that the Cl mixed one has a lower miscibility than Br⁻ ion due to the large difference in the halide ion radius between I⁻ and Cl⁻.⁴⁴

3.4 Actual stoichiometry of perovskite films.

To extract the information of actual stoichiometry in perovskite films, we carried out XPS measurements right after

each film formation. The XPS spectra for the constituent atoms in MAPb(I_{1-y}Cl_y)₃ and MAPb(I_{1-y}Br_y)₃ films are displayed in Figs. 4 and 5, respectively. The Pb 4f_{7/2} BE in MAPb(I_{1-y}Cl_y)₃ film in Fig. 4a appears constant at 138.6 eV, while the initial Pb 4f_{7/2} peak (139.05 eV) in MAPb(I_{1-y}Br_y)₃ film in Fig. 5a is shifted to a lower BE by 0.4 eV with high MAI deposition ratio. The Pb 4f_{7/2} BEs for pristine PbI₂, PbBr₂, and PbCl₂ compounds appear at 138.60, 139.05, and 139.15 eV, respectively (Fig. S4). The BEs exactly follow the order of electronegativity of halogen atoms (Cl > Br > I) bound to Pb. In comparison, the constant Pb 4f_{7/2} BE at 138.6 eV for MAPb(I_{1-y}Cl_y)₃ irrespective of MAI deposition ratio indicates that its local chemical environment does not change from PbI₂. It has no clear evidence for the bonding character of Pb-Cl at all. On the other hand, the continuous change of Pb 4f_{7/2} BE in MAPb(I_{1-y}Br_y)₃ film toward the low BE side with high MAI ratio in Fig. 5a means that the majority of lead halides changes from initial Pb-Br to I-Pb-Br mixed bonds.

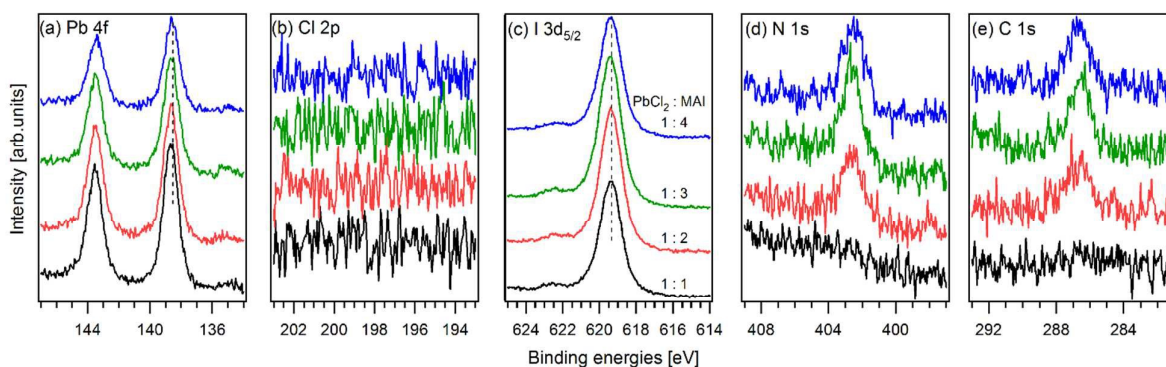


Fig. 4 XPS core level spectra of MAPb(I_{1-y}Cl_y)₃ as a function of deposition ratio between PbCl₂ and MAI precursors.

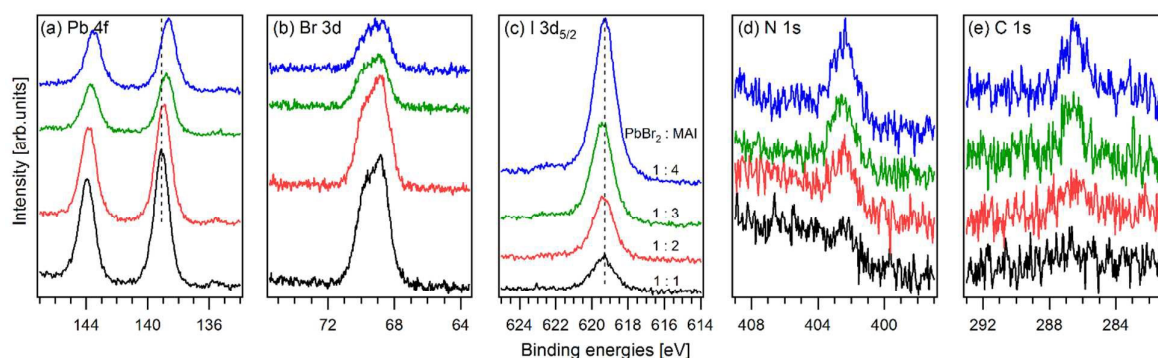


Fig. 5 XPS core level spectra of MAPb(I_{1-y}Br_y)₃ as a function of deposition ratio between PbBr₂ and MAI precursors

Some have reported a metallic Pb 4f_{7/2} peak (~137.0 eV) in solution based perovskite.⁴⁵⁻⁴⁷ The metallic Pb as electron-donor is an avoidable defect but vulnerable to oxygen and moisture, which is one of the vital factors for the perovskite degradation. Thus, the absence of metallic Pb through the present vacuum deposition process facilitates more stable and

impurity-free lead perovskite solar cells in comparison with solution based process.

In Fig. 4b, no meaningful Cl 2p intensity for MAPb(I_{1-y}Cl_y)₃ is observed within the detection limit even though the initial source for perovskite film consists of various compositions of PbCl₂ precursor. That means, the PbCl₂ precursor is dissociated

into Pb^{2+} and 2Cl^- and then most of Cl^- containing compounds are removed during the film formation.

The absence of Cl 2p intensity in the $\text{MAPb}(\text{I}_{1-y}\text{Cl}_y)_3$ film is consistent with the above explanation of constant Pb 4f_{7/2} BE position, unchanged crystal lattice structure, and anomalous IP values. However we verify that the Cl 2p core level peak does appear distinctly under PbCl_2 rich (and only) deposition condition (Fig. S5) although this condition never generates a perovskite crystal formation. On the other hand, the broad Br 3d peak at 3d_{5/2} BE of 68.8 eV arises for $\text{MAPb}(\text{I}_{1-y}\text{Br}_y)_3$ film in Fig. 3b with spin-orbit splitting of 1.05 eV. With the increase of MAI deposition ratio, the Br 3d peak intensity is gradually decreased.

The I 3d_{5/2}, N 1s, and C 1s peaks in Figs. 4c-e and 5c-e appear at 619.4, 402.5, and 286.5 eV, respectively. All the peaks show a singlet feature throughout the PbX_2 and MAI deposition ratios. In particular, as compared to the result for pristine MAI film (Fig. S5), the C 1s and N 1s shows the exactly the same chemical environment of MA moiety in both $\text{MAPb}(\text{I}_{1-y}\text{Cl}_y)_3$ and $\text{MAPb}(\text{I}_{1-y}\text{Br}_y)_3$ films. This means that the fabricated films are free from other carbon contaminants such as residual solvents that might occur in solution process. Thus the present films are suitable for accurate stoichiometry evaluation.

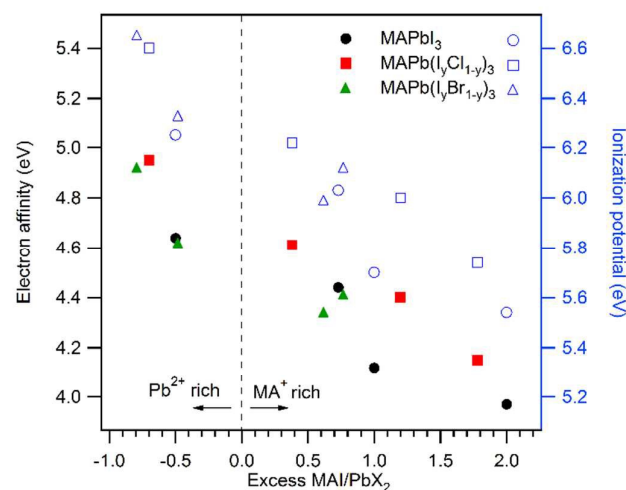


Fig. 6 Excess MA^+ effect on electronic affinity (left axis, solid symbols) and ionization potential (right axis, open symbols) for the mixed halide perovskite films of MAPbI_3 (circles), $\text{MAPb}(\text{I}_{1-y}\text{Cl}_y)_3$ (rectangles), and $\text{MAPb}(\text{I}_{1-y}\text{Br}_y)_3$ (triangles).

Table S1 summarizes the relative atomic composition of constituent elements in all the fabricated films. This quantitative investigation shows that deposition ratio of the precursor does not represent a real stoichiometry of fabricated film. The difference between actual stoichiometry and precursor deposition ratio of the film results from residual reactants and/or natural removal of volatile compounds during the vacuum deposition. For instance, the absence of Cl in the $\text{MAPb}(\text{I}_{1-y}\text{Cl}_y)_3$ film is due to the active removal of MACl compound in gaseous form. Indeed MACl is much more volatile than MABr or MAI .⁴⁸ Moreover, the ideal atomic ratio

of C/X for the perovskite structure is 0.33. When the ratio is lower than this value, no clear crystallization occurs in Fig. 1. Interestingly when the ratio is higher than 0.33, it does not disrupt the crystal structure, but excess MA^+ must exist.

We compare the EA and IP with the excess MA^+ in Fig. 6 where the excess MA^+ is calculated from the atomic ratio of C with respect to Pb, $(\text{C-Pb})/\text{Pb}$. On the left side where the Pb^{2+} is rich compared to MA^+ , the perovskite structure is not assured in Fig. 1. But the right side shows MA^+ rich concentration and the EA is scalable with excess amount of MA^+ , fulfilling the perovskite structure formation. As the excess MA^+ is increased, both the EA and IP are decreased. While the E_g in Fig. 2 shows the subtle change of 0.15 eV at most, the EA and IP show the significant variation of about 0.7 eV depending on atomic composition. Surprisingly they have even a similar slope. Since the IP is the sum of EA and E_g , the EA variation is reflected by thoroughly the IP variation as a result of an electronic effect rather than the variation of E_g by structural effect. The excess MA cation can play a role of positive doping or partial substitution of Pb in the perovskite. However, the MA^+ is out of framework of covalent bonds made of lead halide octagonal structure. This is why the E_g is not changed much but the EA differs a lot. As the conduction band is formed of Pb 6p orbital,⁴³ the relative concentration of Pb^{2+} with respect to MA^+ affects primarily the EA, the energy level of conduction band. Although the organic cation is known to only help with charge neutralization in perovskite structure, its relative concentration can strongly influence the electronic property of film. Since the EA has a large influence on the energy level alignment at photovoltaic film interfaces, the control of EA is of particular importance in the choice of material stack structure and cell efficiency management.

3.5 Surface morphology of halide mixed perovskite films.

In planar type photovoltaic cells, defect-free surface morphology is one of the key factors in order to achieve high performance. So far the solution processed perovskite film is known to have many pinholes that are detrimental to device performance.⁴⁹ Whereas, vacuum deposited perovskite film shows the possibility to offer high-quality smooth surfaces.⁵⁰ We compare the surface morphology and roughness of each mixed-halide perovskite film using AFM in the area of $5\ \mu\text{m} \times 5\ \mu\text{m}$ in Fig. 7. The images for pristine precursor films are compared in Fig. S6. The perovskite films used for the morphology measurement are manufactured by the deposition ratio of 1:4 for PbX_2 and MAI, as those have high purity of perovskite films according to the XRD results in Fig. 1. The root-mean-square roughness (R_{rms}) of the perovskite film surfaces made of PbI_2 and PbCl_2 precursors shows dramatic change from 16.65 nm to 5.72 nm. Even though no post-heat treatment is performed, the $\text{MAPb}(\text{I}_{1-y}\text{Cl}_y)_3$ surface is smooth and flat except for tens-of-nanometer scale protrusions on the flat surface in Fig. 7b. On the other hand, the R_{rms} increases to 21.72 nm by the use of PbBr_2 precursor in Fig. 7c. In comparison, there are large size of hills and troughs on the ARM images in Fig. 7a and c, which makes the surface rougher. In general, the perovskite film morphology becomes largely

smooth by proper post annealing.^{16, 51, 52} This is closely related to solvent evaporation and recrystallization. Vacuum deposition avoids unnecessary solvent evaporation, which generally renders a smooth surface. We suppose the spontaneous MAI removal into gas phase makes the surface further smooth in the formation of $\text{MAPb}(\text{I}_{1-y}\text{Cl}_y)_3$. In contrast, the Br ion generates the rough surface in Fig. 7c possibly because a volatile MABr is hardly formed during the reaction.

Furthermore, one interesting feature of the Br mixed perovskite in Fig. 7c is several spots of lying leaf-like shape (white circles) on the surface. This is the hollow protrusion that makes a highly rough surface.

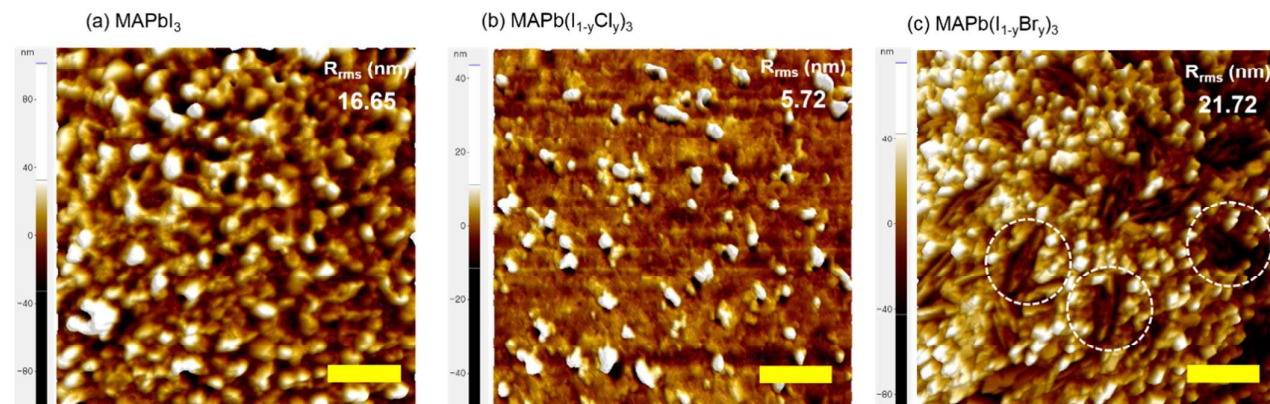


Fig. 7 AFM top view images of mixed halide perovskite films for (a) MAPbI_3 , (b) $\text{MAPb}(\text{I}_{1-y}\text{Cl}_y)_3$, and (c) $\text{MAPb}(\text{I}_{1-y}\text{Br}_y)_3$. Each surface roughness of the perovskite films is noted as root mean-square (R_{rms}) value. Leaf-like protrusions are marked by white circles in (c).

Conclusions

We have fabricated mixed halide perovskite films by simultaneous vacuum deposition of PbX_2 ($X = \text{Cl}, \text{Br}, \text{and I}$) and MAI precursors with various ratios to investigate its influence on electronic properties, chemical composition, crystal structure, and surface morphology. Since the precursors undergo ion exchange to form a perovskite structure, the MAI deposition rate of more than twice the PbX_2 is necessary to make a relatively pure perovskite film. While the $\text{MAPb}(\text{I}_{1-y}\text{Cl}_y)_3$ shows negligible amount of Cl in the film, the $\text{MAPb}(\text{I}_{1-y}\text{Br}_y)_3$ reveals the Br incorporation in the compound and the corresponding lattice space change. The IP and EA decrease with the MA^+ amount with respect to Pb^{2+} in the film, though the E_g does not change much. This controllability of electronic property with similar E_g is one of excellent advantages of mixed halide perovskite films for solar cell manufacturing. Vacuum-processed film surfaces are generally smooth in particular for $\text{MAPb}(\text{I}_{1-y}\text{Cl}_y)_3$. Based on the above characterization of perovskite film, we construct a strategy to control actual stoichiometry, crystal structure, bandgap, and even morphological property for a desirable mixed halide perovskite device.

Acknowledgements

We acknowledge the support from National Research Foundation (NRF) grant No. 2014-007296 and the New &

Renewable Energy of the Korea Institute of Energy Technology Evaluation and Planning (KETEP) grant funded by the Korea government MKE (20123010010150). We thank Mr. In Young Jung and Dr. Chang Soo Kim at KRISS for helping us with XRD.

References

1. E. J. Juarez-Perez, R. S. Sanchez, L. Badia, G. Garcia-Belmonte, Y. S. Kang, I. Mora-Sero and J. Bisquert, *J. Phys. Chem. Lett.*, 2014, **5**, 2390-2394.
2. N.-G. Park, *J. Phys. Chem. Lett.*, 2013, **4**, 2423-2429.
3. W.-J. Yin, J.-H. Yang, J. Kang, Y. Yan and S.-H. Wei, *J. Mater. Chem. A*, 2015, **3**, 8926-8942.
4. M. I. Dar, N. Arora, P. Gao, S. Ahmad, M. Grätzel and M. K. Nazeeruddin, *Nano Lett.*, 2014, **14**, 6991-6996.
5. Q. Wang, Y. Shao, Q. Dong, Z. Xiao, Y. Yuan and J. Huang, *Energy Environ. Sci.*, 2014, **7**, 2359-2365.
6. J. Burschka, N. Pellet, S. J. Moon, R. Humphry-Baker, P. Gao, M. K. Nazeeruddin and M. Grätzel, *Nature*, 2013, **499**, 316-319.
7. I. E. Castelli, J. M. García-Lastra, K. S. Thygesen and K. W. Jacobsen, *APL Mater.*, 2014, **2**, 081514.
8. J. H. Noh, S. H. Im, J. H. Heo, T. N. Mandal and S. I. Seok, *Nano Lett.*, 2013, **13**, 1764-1769.
9. E. T. Hoke, D. J. Slotcavage, E. R. Dohner, A. R. Bowring, H. I. Karunadasa and M. D. McGehee, *Chem. Sci.*, 2015, **6**, 613-617.
10. L. Etgar, P. Gao, Z. Xue, Q. Peng, A. K. Chandiran, B. Liu, M. K. Nazeeruddin and M. Grätzel, *J. Am. Chem. Soc.*, 2012, **134**, 17396-17399.
11. J. Y. Jeng, Y. F. Chiang, M. H. Lee, S. R. Peng, T. F. Guo, P. Chen and T. C. Wen, *Adv. Mater.*, 2013, **25**, 3727-3732.
12. K. Liang, D. B. Mitzi and M. T. Prikas, *Chem. Mater.*, 1998, **10**, 403-411.

13. P. Docampo, J. M. Ball, M. Darwich, G. E. Eperon and H. J. Snaith, *Nat. Commun.*, 2013, **4**, 2761-2766.
14. G. E. Eperon, V. M. Burlakov, P. Docampo, A. Goriely and H. J. Snaith, *Adv. Funct. Mater.*, 2014, **24**, 151-157.
15. Y. J. Jeon, S. Lee, R. Kang, J. E. Kim, J. S. Yeo, S. H. Lee, S. S. Kim, J. M. Yun and D. Y. Kim, *Sci. Rep.*, 2014, **4**, 6953-6959.
16. M. Liu, M. B. Johnston and H. J. Snaith, *Nature*, 2013, **501**, 395-398.
17. G. Xing, N. Mathews, S. Sun, S. S. Lim, Y. M. Lam, M. Grätzel, S. Mhaisalkar and T. C. Sum, *Science*, 2013, **342**, 344-347.
18. S. D. Stranks, G. E. Eperon, G. Grancini, C. Menelaou, M. J. P. Alcocer, T. Leijtens, L. M. Herz, A. Petrozza and H. J. Snaith, *Science*, 2013, **342**, 341-344.
19. S. Colella, E. Mosconi, P. Fedeli, A. Listorti, F. Gazza, F. Orlandi, P. Ferro, T. Besagni, A. Rizzo, G. Calestani, G. Gigli, F. De Angelis and R. Mosca, *Chem. Mater.*, 2013, **25**, 4613-4618.
20. P. Docampo, F. C. Hanusch, S. D. Stranks, M. Döblinger, J. M. Feckl, M. Ehrensperger, N. K. Minar, M. B. Johnston, H. J. Snaith and T. Bein, *Adv. Energy Mater.*, 2014, **4**, 1400355.
21. G. Grancini, S. Marras, M. Prato, C. Giannini, C. Quarti, F. De Angelis, M. De Bastiani, G. E. Eperon, H. J. Snaith, L. Manna and A. Petrozza, *J. Phys. Chem. Lett.*, 2014, **5**, 3836-3842.
22. J. You, Z. Hong, Y. Yang, Q. Chen, M. Cai, T.-B. Song, C.-C. Chen, S. Lu, Y. Liu, H. Zhou and Y. Yang, *ACS Nano*, 2014, **8**, 1674-1680.
23. B. Philippe, B.-W. Park, R. Lindblad, J. Oscarsson, S. Ahmadi, E. M. J. Johansson and H. Rensmo, *Chem. Mater.*, 2015, **27**, 1720-1731.
24. T.-W. Ng, C.-Y. Chan, M.-F. Lo, Z. Q. Guan and C.-S. Lee, *J. Mater. Chem. A*, 2015, **3**, 9081-9085.
25. H. Yu, F. Wang, F. Xie, W. Li, J. Chen and N. Zhao, *Adv. Funct. Mater.*, 2014, **24**, 7102-7108.
26. S. I. Mohammed, Y. Al-Douri, U. Hashim, N. M. Ahmed and R. Al-Gaashani, *Can. J. Phys.*, 2013, **91**, 826-832.
27. D. H. Cao, C. C. Stoumpos, C. D. Malliakas, M. J. Katz, O. K. Farha, J. T. Hupp and M. G. Kanatzidis, *APL Mater.*, 2014, **2**, 1-7.
28. T.-B. Song, Q. Chen, H. Zhou, S. Luo, Y. Yang, J. You and Y. Yang, *Nano Energy*, 2015, **12**, 494-500.
29. Y. Ma, L. Zheng, Y. H. Chung, S. Chu, L. Xiao, Z. Chen, S. Wang, B. Qu, Q. Gong, Z. Wu and X. Hou, *Chem. Commun.*, 2014, **50**, 12458-12461.
30. Y. Zhao and K. Zhu, *J. Mater. Chem. A*, 2015, **3**, 9086-9091.
31. Q. Chen, H. Zhou, T. B. Song, S. Luo, Z. Hong, H. S. Duan, L. Dou, Y. Liu and Y. Yang, *Nano Lett.*, 2014, **14**, 4158-4163.
32. N. Tripathi, M. Yanagida, Y. Shirai, T. Masuda, L. Han and K. Miyano, *J. Mater. Chem. A*, 2015, **3**, 12081-12088.
33. T. Ma, M. Cagnoni, D. Tadaki, A. Hirano-Iwata and M. Niwano, *J. Mater. Chem. A*, 2015, **3**, 14195-14201.
34. P. Schulz, E. Edri, S. Kirmayer, G. Hodes, D. Cahen and A. Kahn, *Energy Environ. Sci.*, 2014, **7**, 1377-1381.
35. B. Suarez, V. Gonzalez-Pedro, T. S. Ripolles, R. S. Sanchez, L. Otero and I. Mora-Sero, *J. Phys. Chem. Lett.*, 2014, **5**, 1628-1635.
36. S. A. Kulkarni, T. Baikie, P. P. Boix, N. Yantara, N. Mathews and S. Mhaisalkar, *J. Mater. Chem. A*, 2014, **2**, 9221-9225.
37. S. Aharon, A. Dymshits, A. Rotem and L. Etgar, *J. Mater. Chem. A*, 2014, **3**, 9171-9178.
38. S. A. Bretschneider, J. Weickert, J. A. Dorman and L. Schmidt-Mende, *APL Mater.*, 2014, **2**, 081506.
39. J. H. Im, I. H. Jang, N. Pellet, M. Grätzel and N. G. Park, *Nat. Nanotechnol.*, 2014, **9**, 927-932.
40. W. A. Laban and L. Etgar, *Energy Environ. Sci.*, 2013, **6**, 3249-3253.
41. H. Hu, D. Wang, Y. Zhou, J. Zhang, S. Lv, S. Pang, X. Chen, Z. Liu, N. P. Padture and G. Cui, *RSC Adv.*, 2014, **4**, 28964-28967.
42. K. Tanaka, T. Takahashi, T. Ban, T. Kondo, K. Uchida and N. Miura, *Solid State Commun.*, 2003, **127**, 619-623.
43. K. T. Butler, J. M. Frost and A. Walsh, *Mater. Horiz.*, 2014, **2**, 228-231.
44. E. L. Unger, A. R. Bowring, C. J. Tassone, V. L. Pool, A. Gold-Parker, R. Cheacharoen, K. H. Stone, E. T. Hoke, M. F. Toney and M. D. McGehee, *Chem. Mater.*, 2014, **26**, 7158-7165.
45. B. Conings, L. Baeten, C. De Dobbelaere, J. D'Haen, J. Manca and H. G. Boyen, *Adv. Mater.*, 2014, **26**, 2041-2046.
46. R. Lindblad, D. Bi, B.-w. Park, J. Oscarsson, M. Gorgoi, H. Siegbahn, M. Odelius, E. M. J. Johansson and H. Rensmo, *J. Phys. Chem. Lett.*, 2014, **5**, 648-653.
47. R. Lindblad, N. K. Jena, B. Philippe, J. Oscarsson, D. Bi, A. Lindblad, S. Mandal, B. Pal, D. D. Sarma, O. Karis, H. Siegbahn, E. M. J. Johansson, M. Odelius and H. Rensmo, *J. Phys. Chem. C*, 2015, **119**, 1818-1825.
48. Y. Zhao and K. Zhu, *J. Am. Chem. Soc.*, 2014, **136**, 12241-12244.
49. W. Zhang, M. Saliba, D. T. Moore, S. K. Pathak, M. T. Hörantner, T. Stergiopoulos, S. D. Stranks, G. E. Eperon, J. A. Alexander-Webber, A. Abate, A. Sadhanala, S. Yao, Y. Chen, R. H. Friend, L. A. Estroff, U. Wiesner and H. J. Snaith, *Nat. Commun.*, 2015, **6**, 6142-6151.
50. T. Salim, S. Sun, Y. Abe, A. Krishna, A. C. Grimsdale and Y. M. Lam, *J. Mater. Chem. A*, 2015, **3**, 8943-8969.
51. A. Dualeh, N. Tétreault, T. Moehl, P. Gao, M. K. Nazeeruddin and M. Grätzel, *Adv. Funct. Mater.*, 2014, **24**, 3250-3258.
52. F. X. Xie, D. Zhang, H. Su, X. Ren, K. S. Wong, M. Grätzel and W. C. H. Choy, *ACS Nano*, 2014, **9**, 639-646.